Cranfield
UNIVERSITY

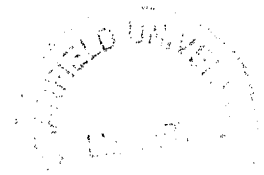# Solution of the Navier-Stokes Equations for aerofoils undergoing inplane oscillations

Scott Shaw

Department of Aerospace Science
College of Aeronautics
Cranfield University
Cranfield
Bedford MK43 0AL
England

Cranfield

Solution of the Navier-Stokes Equations for aerofoils undergoing inplane oscillations.

Scott Shaw

Department of Aerospace Science
College of Aeronautics
Cranfield University
Cranfield, Bedford MK43 0AL. England

£8

Abstract

Although a full simulation of the flow field generated around helicopter rotor blades in forward flight requires consideration of many complex interacting flow phenomena, such as fluctuations in the velocity and incidence of the oncoming flow, three dimensional effects, moving shock waves, shock induced separation and dynamic stall, considerable physical insight may be obtained by removing the influence of many of these phenomena and studying the simplified flows which result.

In the present work the problems of moving shock waves and shock induced separation commonly encountered on the advancing side of helicopter rotor blades during forward flight are addressed by examining the behaviour of the flow field around aerofoils undergoing inplane oscillations, of the form $M_\infty = M_1(1+\mu\sin(\omega t))$, at constant angles of incidence.

In this paper a method for the solution of the thin layer Navier-Stokes equations for aerofoils undergoing inplane oscillations is presented. The sensitivity of the method to a number of the main control parameters is investigated and the results of preliminary calculations and validation with experimental data are presented.

1. Introduction

Although a full simulation of the flow field generated around helicopter rotor blades in forward flight requires consideration of many complex interacting flow phenomena, such as fluctuations in the velocity and incidence of the oncoming flow, three dimensional effects, moving shock waves, shock induced separation and dynamic stall, considerable physical insight may be obtained by removing the influence of many of these phenomena and studying the simplified flows which result.

In the present work the problems of moving shock waves and shock induced separation commonly encountered on the advancing side of helicopter rotor blades during forward flight are addressed by examining the behaviour of the flow field around aerofoils undergoing inplane oscillations, of the form $M_\infty = M_1(1+\mu\sin(\omega t))$, at constant angles of incidence.

The behaviour of aerofoils undergoing pure inplane oscillations[1,2,3] and combined translation/pitch[2,3] oscillations has been investigated by Favier and Maresca at low free stream velocities. It was found that the flow field could be considered to be essentially quasi-steady for angles of incidence below that of static stall. For incidences through and beyond that at which static stall occurred large increases in lift, drag and pitching moment coefficients were observed together with a phase delay in the occurrence of maximum lift coefficient. The resulting flow field was found to be strongly dependent upon the reduced frequency ($k=c\omega/2V_\infty$) and the reduced amplitude ($A\omega/V_\infty$). Instantaneous data and flow visualisation[1] show that the boundary layer becomes reattached, following separation, while the aerofoil is accelerating forwards. Such a reattachment leads to the formation of a large separation bubble over the forward part of the aerofoil similar to that observed during the dynamic stall of aerofoils oscillating in pitch.

A wide range of analytical approaches are available for calculating unsteady, inviscid, incompressible flow. Van der Waal and Leischmann[4] have applied a number of these models to the problem of inplane oscillations with some success and have been able to demonstrate excellent agreement with results obtained from an Euler code operating at low free stream Mach number.

At the present time no experimental results are available for aerofoils undergoing inplane oscillations at transonic Mach numbers. Consequently the validation of current computational methods is unsatisfactory and is performed by appealing to the underlying flow physics, comparison with existing computational approaches and comparison with three dimensional test data.

Current computational approaches are restricted to the solution of the unsteady Euler equations. In Reference (5) Habibie et al transform the governing equations onto a non-inertial frame of reference. This approach is however restricted to inplane oscillations and a more general approach is adopted by Lerat and Sides[6] and Lin and Pahlke[7] who solve the Euler equations in general moving co-ordinates and are able to obtain very good agreement with the published three dimensional experimental data of Phillipe and Chattot[8].

A finite volume method based upon Oshers flux difference splitting was developed by Qin et al[18] for both two dimensional parabolised Navier-Stokes equations and three dimensionsal Navier-Stokess solutions for high speed flows (in the transonic and hypersonic Mach number range) viscous flow problems. It has been demonstrated[19,20] that such a high resolution scheme can capture both shock waves and shear layers accurately allowing the reliable prediction of shock wave-boundary layer interactions. Badcock[9,10] has extended the above approach to unsteady problems using the AF-CGS method for the time discretisation. It has been applied to unsteady pitching aerofoils in transonic flow.

In the present work the above methodology has been extended for the study of the transonic flow around aerfoils undergoing inplane oscillations. For some difficult cases GMRES was used insteady of CGS because of its improved convergence behaviour. In the following sections the computer code AF-CGS is described and preliminary results are presented.

2. AF-CGS

The compressible formulation of the thin layer Navier-Stokes equations for generalised moving co-ordinates may be given in strong conservation form as,

$$\frac{\partial Q}{\partial t} + \frac{\partial F}{\partial \xi} + \frac{\partial G}{\partial \eta} = \frac{1}{Re}\frac{\partial S}{\partial \eta} \tag{1}$$

in which Q is the vector of conservative variables, F and G are the inviscid fluxes and S is the viscous flux. These terms are given by,

$$Q = \frac{1}{J}\begin{bmatrix} \rho \\ \rho u \\ \rho v \\ e \end{bmatrix}, \quad F = \frac{1}{J}\begin{bmatrix} \rho U \\ \rho uU + \xi_x P \\ \rho vU + \xi_y P \\ U(e+P) - P\xi_t \end{bmatrix}, \quad G = \frac{1}{J}\begin{bmatrix} \rho V \\ \rho uV + \eta_x P \\ \rho vV + \eta_y P \\ V(e+P) - P\eta_t \end{bmatrix},$$

$$\tag{2}$$

$$S = \frac{1}{J}\begin{bmatrix} 0 \\ \mu m_1 u_\xi + \left(\frac{\mu}{3}\right)m_2\xi_x \\ \mu m_1 v_\xi + \left(\frac{\mu}{3}\right)m_2\xi_y \\ \mu m_1 m_3 + \left(\frac{\mu}{3}\right)m_2\left(\xi_x u + \xi_y v\right) \end{bmatrix}$$

Here,

$$m_1 = \xi_x^2 + \xi_y^2, \quad m_2 = \eta_x^2 + \eta_y^2 \text{ and } m_3 = \frac{\left(u^2 + v^2\right)}{2} + \frac{c_\xi^2}{Pr(\gamma - 1)}.$$

and J is the determinant of the transformation between the physical (x,y) plane and the computational (ξ, η) plane. Density, the two components of velocity, energy, pressure, Prandtl number, Reynolds number, speed of sound, viscosity (with a turbulent contribution calculated using the Baldwin-Lomax turbulence model[11]) and the ratio of specific heats are denoted by ρ, u, v, e, P, Pr, Re, c, μ and γ respectively. In the above equations J is the Jacobian of the transformation from the physical to computational planes and U and V are the contra-variant velocities defined as,

$$U = \xi_x\left(u - x_t\right) + \xi_y\left(v - y_t\right)$$

$$\tag{3}$$

$$V = \eta_x(u - x_t) + \eta_y(v - y_t)$$

where x_t and y_t represent the components of grid velocity.

Applying a backwards finite difference in time to the governing equation (1) gives,

$$\frac{Q^{n+1} - Q^n}{\Delta t} + \frac{\partial F^{n+1}}{\partial \xi} + \frac{\partial (G - S)^{n+1}}{\partial \eta} = 0 \tag{4}$$

The flux vectors are linearised about time level n+1 using expressions of the form,

$$\frac{\partial F^{n+1}}{\partial \xi} = \frac{\partial F^n}{\partial \xi} + \frac{\partial F_\xi}{\partial Q}^n \left(Q^{n+1} - Q^n \right) + O(\Delta t^2) \tag{5}$$

Substituting for the flux vectors in Equation (4) a fully implicit method is obtained thus,

$$\left(I + \Delta t \frac{\partial F_\xi^n \cdot}{\partial Q} + \Delta t \frac{\partial (G - S)_\eta^n \cdot}{\partial Q} \right) \Delta Q^n = \frac{\Delta t}{Re} \left(S_\eta^n - F_\xi^n - G_\eta^n \right) \tag{6}$$

in which $Q^{n+1} = Q^n + \Delta Q^n$.

This implicit formulation is unconditionally stable allowing the use of large time steps. The maximum available time step is determined from a consideration of the linearisation error contained in Equation (5).

Oshers approximate Riemann solver[12] is used for the spatial discretisation of the inviscid flux terms contained in Equation (6) while central differences are employed for the spatial discretisation of the viscous flux term. This approach to the spatial discretisation is based upon that proposed and tested by Qin et al[19,20] and it has been demonstrated that both shock waves and shear layers are calculated accurately. Higher order spatial accuracy is achieved using MUSCL interpolation[13] while Von Albadas flux limiter is utilised for the removal of the spurious oscillations commonly found in the region of strong discontinuities, for example shock waves.

For any implicit method the calculation, storage and solution of the large, sparse non-symmetric matrix (the Jacobian matrix) which appears on the left hand side of Equation (6) are important issues. The calculation of the exact flux Jacobians involves the use of analytical expressions and the chain rule thus,

$$\frac{\partial F}{\partial Q_i} = \frac{\partial F}{\partial \hat{Q}_L} \frac{\partial \hat{Q}_L}{\partial Q_L} \frac{\partial Q_L}{\partial Q_i} + \frac{\partial F}{\partial \hat{Q}_R} \frac{\partial \hat{Q}_R}{\partial Q_R} \frac{\partial Q_R}{\partial Q_i} \tag{7}$$

where $\hat{Q} = \begin{bmatrix} \rho & u & v & P \end{bmatrix}^T$ and $\frac{\partial Q_L}{\partial Q_i}, \frac{\partial Q_R}{\partial Q_i}$ are calculated from the MUSCL interpolation. It is readily apparent that the resulting expressions for the flux Jacobians are complicated. Optimised, error free code has been produced using the symbolic algebra manipulation package Reduce. The calculation of the flux Jacobians in this

way is significantly more expensive (both in terms of CPU time and storage requirement) than a numerical approach. The use of numerical and analytical flux Jacobians is considered in detail by Vanden and Orkwis[14].

Having obtained the flux Jacobians Equation (6) results in a system of linear equations,

$$[A]\{x\}=\{b\} \tag{8}$$

Direct solvers, such as LU decomposition, are inappropriate for problems of this size and consequently iterative methods must be employed. The selection of an appropriate iterative scheme is based on a wide range of criterion which include robustness, efficiency and expense. In the current approach CGS[15] is used to solve Equation (8). The system matrix, the matrix [A] on the left hand side of Equation (8), is generally ill-conditioned for this class of problems which has severe consequences for the convergence behaviour of CGS (and most alternate iterative solvers).

In order to improve the condition of the system matrix, and hence the convergence behaviour of the iterative solver, pre-conditioning is required. We seek a pre-conditioning matrix which when used to pre-multiply Equation (8) results in a new system of equations,

$$\left[C^{-1}\right][A]\{x\} = \left[\tilde{A}\right]\{x\} = \left[C^{-1}\right]\{b\} \tag{9}$$

which is more amenable to solution by iterative techniques. In general the condition of the matrix improves as the system matrix becomes more diagonally dominant (i.e. as it becomes closer to the identity matrix) . We therefore require that,

$$\left[\tilde{A}\right] = [I]$$

$$\text{i.e.} \quad \left[C^{-1}\right] \approx \left[A^{-1}\right]$$

In order to obtain a suitable approximation for the inverse of the system matrix we note that Equation (6) may be approximately factored to obtain,

$$\left(I + \Delta t \frac{\partial F_\xi \cdot}{\partial Q}\right)\left(I + \Delta t \frac{\partial (G-S)_\eta \cdot}{\partial Q}\right)\Delta Q = \Delta t\left(S_\eta - F_\xi - G_\eta\right) \tag{10}$$

Equation (10) is the basis of the well known alternating direction implicit method[16] and may be solved for ΔQ by first sweeping in the η-direction and then in the ξ-direction. This approach is efficient (requiring the solution of a block diagonal system of linear equations for each i and j) but introduces a factorisation error which places restrictions on the maximum size of time step which can be considered. When used to precondition Equation (8) this factorisation error is of little importance (although it does provide a good measure of the accuracy of the approximation to the inverse of the system matrix). In most iterative methods the system matrix is only

required as a matrix-vector product and ADI pre-conditioning can be introduced by solving for {s} in,

$$\left(I + \Delta t \frac{\partial F_\xi \cdot}{\partial Q}\right)\left(I + \Delta t \frac{\partial (G - S)_\eta \cdot}{\partial Q}\right)\{s\} = \Delta t[A]\{x\} \qquad (11)$$

where $[A]\{x\}$ is the matrix-vector product for which $[C^{-1}][A]\{x\}$ is required. Over the course of one time step Equation (11) is solved for a number of right hand sides and so the operations required to invert the approximate factors on the left hand side of Equation (11) are stored leading to a reduced operations count (although this increased efficiency is achieved at the expense of a considerable storage penalty).

The choice of time step can greatly influence the conditioning of the system matrix with decreasing time step leading to greater diagonal dominance. The most efficient implementation of CGS will therefore seek to balance the cost of solving the linear system and the number of outer iterations (time steps) which are required.

Boundary conditions are specified at the far field boundary by consideration of the characteristic solutions. For boundaries at which the flow is subsonic extrapolated and free stream Riemann invariants of the form,

$$R = V_n - \frac{2c}{\gamma - 1} \qquad (12)$$

are used to obtain the normal velocity and local speed of sound using the following relationships,

$$V_n = \frac{1}{2}\left(R_e - R_\infty\right)$$

$$\qquad (13)$$

$$c = \frac{\gamma - 1}{4}\left(R_e + R_\infty\right)$$

Here the subscripts denote extrapolated and far field values of the Riemann invariant. At outflow boundaries the tangential velocity and entropy are determined by extrapolation from the interior of the computational domain while at inflow boundaries this information is specified using free stream values. For supersonic boundaries the required information is either all extrapolated (outflow) or all specified (inflow). At the surface of the aerofoil velocity components are determined by applying the no-slip condition while pressure and temperature are calculated by assuming a normal pressure gradient at the wall and an iso-thermal wall respectively.

3. Grid Generation

The computational grid is created by mapping a uniformly distributed rectangular mesh onto the physical domain. The method adopted is based upon that proposed by Eriksson which produces an algebraic C-type mesh around the aerofoil, this approach is described in Reference (17) by Gaitonde and Fiddes.

The mapping is given by,

$$F(\xi,\eta) = \alpha_1^0 F(0,\eta) + \alpha_1^1 \frac{\partial F}{\partial \xi}(0,\eta) + \alpha_2^0 F(1,\eta) \tag{14}$$

where $\alpha_1^0, \alpha_1^1, \alpha_2^0$ are weighting functions and $\xi=0$ and $\xi=1$ correspond to the aerofoil surface (including the wake cut line) and the far field boundaries respectively. The derivative term is introduced in Equation (14) to give some control over the direction with which grid lines leave the aerofoil surface. The weighting functions are chosen such that,

$$\alpha = \frac{e^{kx} - 1 - kx}{e^k - 1 - k}$$

$$\alpha_1^0 = 1 - \alpha \tag{15}$$

$$\alpha_1^1 = x - \alpha$$

$$\alpha_2^0 = \alpha$$

and produce an exponential stretching of the grid points between the bounding surfaces. Additional control of the mesh spacing can be achieved by specifying an intermediate variable, denoted by x in Equation (15). For $x=\xi$ Equation (14) reduces to the original scheme of Eriksson which does not always produce satisfactory results. In the present code an intermediate stretching function,

$$x = P\eta + (1-P)\left[1 - \frac{\tanh(Q(\eta-1))}{\tanh(Q)}\right] \tag{16}$$

is adopted. Control of the normal spacing of grid points is achieved by varying the values of K, P and Q.

4. Unsteady grid motion

For aerofoils which are undergoing unsteady motions (such as inplane and pitching oscillations) it is convenient to use an unsteady grid. While the inertial frame of reference (x,y,t) is fixed in space the computational grid (ξ,η,t) is moving (because it is attached to the moving aerofoil). In order to relate the grid motion with the inertial frame of reference grid velocity terms, such as those found in Equation (3), are introduced.

The grid velocity terms can be specified either analytically, or by comparing the position of the current grid with the position at the previous time step. In practice either approach is acceptable and a decision is often made on the basis of the convenience with which an analytical expression can be obtained. In aeroelastic calculations the latter approach is most often adopted because of the difficulty in providing an analytical expression for the surface deformation while for rigid aerofoil motions ,such as inplane oscillations, the analytical approach is often most convenient.

For the case of a helicopter rotor blade represented by inplane oscillations of an aerofoil, the rotational velocity of the rotor provides a mean flow condition while the forward flight speed is represented by oscillations. The grid velocity terms are then defined by,

$$x_t = -\mu \sin(kt) \quad \text{and} \quad y_t = 0 \tag{17}$$

where μ is the advance ratio (the ratio of the forward flight speed to the local rotational velocity) and k is the reduced frequency (which in this case is given by the ratio of the local chord to the spanwise position of the blade section).

These expressions may be added to those already available in AF-CGS for pitching oscillations (which are calculated by comparing grids at consecutive time steps) provided that the rotation is carried out relative to some fixed point on the aerofoil. If this is not the case and the rotation is carried out about a point which does not move with the aerofoil then the combined effects of translation and rotation are non-linear and the problem is further complicated.

5. Parameter tests

Calculations were performed using the modified AF-CGS method for the flow around a NACA 0012 aerofoil undergoing inplane oscillations, described by $M_\infty = 0.5335(1 + 0.5778\sin(0.8t))$, at a fixed angle of incidence of 0.25 degrees. Calculations were performed on the standard (153 grid points in the streamwise direction, 100 around the aerofoil, and 48 grid points in the surface normal direction) grids shown in Figures (8b) and (9) for the Euler and Navier-Stokes equations respectively. Two cycles of the aerofoil motion were calculated with 600 time steps per cycle and a convergence tolerance of 0.005 on the linear solver. In the following section the sensitivity of these calculations to a number of the main AF-CGS parameters is investigated, while in section (6) a more general discussion of the numerical results together with a comparison with experimental data is presented.

Despite the unconditional stability of the present implicit approach the choice of time step, Δt, remains of great practical importance due to the influence which this parameter has on both the overall accuracy and efficiency of the current numerical method. In Figure (1) results are presented which show the sensitivity of computed lift coefficient (based on the average free stream velocity) to variations in the number of iterations performed for each full cycle of the aerofoil motion. Good agreement was found between the results of the three calculations over most of the cycle which suggests that in general the choice of time step (in the range considered) does not significantly affect the overall accuracy of the solution. Perhaps of greater significance however, is the poor agreement which is found for a limited range of azimuth angles close to 220 degrees. The poor resolution of this feature of the flow suggests that the time scale of the underlying flow physics is much smaller than the larger time steps which have been employed. Further calculations performed for 200, 400, 500 and 1000 time steps per cycle support this hypothesis and have shown that as the time step is reduced the calculation becomes increasingly insensitive to the choice of this parameter, eventually converging to a solution which does not change with further changes in time step.

While the accuracy of the method and the ability to resolve the flow physics fully are important experience has shown that the choice of a practical minimum time step is determined not by such considerations, but by the stability and efficiency of the linear solver which is employed. For the conjugate gradient type methods employed in the current approach efficiency and stability are strongly dependent upon the condition of the preconditioned Jacobian matrix of the linear system which must be solved.

For time accurate implicit methods the condition of the Jacobian matrix is heavily influenced by the choice of time step as this parameter occurs in the denominator of the leading diagonal, consequently large time steps will result in an ill conditioned system of equations (the Jacobian matrix is less diagonally dominant) while smaller time steps lead to relatively well conditioned systems of equations (the

Jacobian matrix becomes increasingly diagonally dominant).[1] The factorisation error which is associated with the ADI preconditioning employed in the current method , which can be shown to be of the order of Δt^2 , provides a good indication of how well ADI approximates the linear system. The order of the truncation error suggest that as the time step is reduced in size the effectiveness of ADI preconditioning should increase. The improved condition of the preconditioned Jacobian matrix with reduced time step is demonstrated by the results presented in Figure (2) which show the number of iterations of CGS required to solve the system of linear equations which result from the choice of different time steps.

Unfortunately the improvements in the efficiency of CGS which result from reductions in the time step must be balanced against the overall cost of the calculation. We expect that some optimum value arises for the time step above which the gains in the efficiency of CGS are outweighed by an increase in the number of outer iterations and below which the reduction in the number of outer iterations is outweighed by the increased cost of CGS. In Figure (3) results are presented which show the total time required to calculate two full cycles of the aerofoil motion against the number of iterations required for each cycle (which is inversely proportional to the size of time step). The results show that the expected optimum value does indeed exist and occurs at around 500 iterations per cycle for this calculation. The occurrence of such minima has been found to depend strongly on the condition of the Jacobian matrix and is therefore strongly case dependent.

The tolerance which is placed upon the convergence of the conjugate gradient solver may have important consequences for the overall accuracy of the method. In AF-CGS the initial 'guess' for the solution of the system of equations required by the conjugate gradient method is obtained using ADI, this approach is adopted because it can reduce significantly the work of the linear solver (at no extra cost as this result is required for the preconditioned right hand side) when compared to alternate starting strategies as the initial solution may be relatively close to the true solution. Low convergence tolerances will therefore produce a final result which is close to that obtained by ADI alone, which for larger time steps may have important effects on accuracy, while for higher convergence tolerances the solution will approach that of the unfactored equations. In Figure (4) the calculated lift coefficients (based on average velocity) are presented for calculations performed using several convergence tolerances (from one to three orders of reduction in the residual norm). The results indicate very little sensitivity of the method to changes in the convergence criteria. This result is unexpected and may possibly be explained by the fact that a single iteration of CGS may reduce the residual much further than is required by the tolerance criteria, i.e. calculations performed with lower convergence criteria may also satisfy the more stringent convergence tolerances of the other calculations.

In Figure (5) results of similar Navier-Stokes calculations performed for a NACA 0012 aerofoil at an incidence of $0°$ in an oscillating free stream described by $M_\infty = 0.536\big(1 + 0.61\sin(0.185t)\big)$ are presented. It would be expected that the

---

[1] This property of the Jacobian matrix is used in AF-CGS as the basis of a strategy for overcoming problems which arise when the convergence of the linear solver becomes stalled.

calculated lift coefficient for this case would be close to zero as the flow conditions are symmetric. We observe however, that for low tolerances, 0.005, the flow is non-symmetric, as revealed by a relatively high lift coefficient at around $\psi = 90°$. An examination of the flow field reveals that the flow is indeed symmetric until the shock wave first appears. As the flow field develops further the shock wave on the lower surface begins to move forwards towards the leading edge more quickly than that on the upper surface and a non-symmetric flow is established. The unexpected behaviour of the flow field for this case is clearly an artefact of the numerical method as more stringent tolerances, 0.0005 and 0.00005, result in very different calculated lift coefficients. Euler calculations performed for the same flow conditions do not exhibit a sensitivity to this parameter which suggests that care should be taken in selecting an appropriate value for this parameter for Navier-Stokes calculations.

Finally the influence of the computational grid was investigated. The parameters tested were the grid density (number of grid points) and the location of the far field boundaries.

In Figure (6) calculated lift coefficients are presented for Euler calculations performed with successively finer grids ,Figures (8a) to (8c), having 101x24 (50 points on the aerofoil), 153x48 (100 points on the aerofoil) and 259x96 (200 points on the aerofoil) grid points in the streamwise and surface normal directions respectively. The coarse grid calculation (101x48) clearly fails to resolve the flow adequately and is particularly poor for azimuth angles close to 90°, where shock waves occur, and 180° where the flow is separated. A doubling of the number of grid points in both grid directions leads to a dramatic improvement in the quality of the calculated results. The medium grid calculation is able to resolve all of the flow physics which are captured by the finer grid (259x96) calculation. The medium grid calculation does however consistently underestimate the value for the lift coefficient obtained using the finer grid and is particularly poor for azimuth angles close to $C_{L\,max.}$ this poor agreement can be attributed to a poorer resolution of shock wave location in the medium grid calculation.

Refinements of the computational grid, and grid stretching, have been found to influence the convergence behaviour of the linear solver, with finer grid calculations exhibiting a poorer rate of convergence than that found on a coarser grid. It is well known that increasing the size of the system which the linear solver is required to solve reduces the rate of convergence of the linear solver and so this behaviour is not unexpected.

Unlike the steady version of AF-CGS the unsteady AF-CGS method does not includes corrections to the calculated data for the location of the far stream boundary. Consequently investigations were carried out to determine the sensitivity of the calculated results to this parameter. The effects of doubling the location of the far field boundary from 20 to 40 chord lengths are presented in Figure (7). Over the first few cycles of the aerofoil motion agreement between the calculations is very poor, this is a consequence of the poor convergence of the initial steady calculation for a far field boundary located at 20 chord lengths from the aerofoil. As the unsteady calculations converge to the final cyclical result agreement between the calculations

improves until only very small differences are observed in the values of lift coefficient at local maxima and minima. It is suggested that a value of 20 chord lengths should be used to fix the location of the far field boundary from the aerofoil surface.

6. Validation.

In Reference (8) Phillipe and Chattot present experimental measurements for several spanwise sections of a non-lifting rotor blade in forward flight. The rotor blade, which has a symmetric NACA 00XX profile, was tested with a tip speed of 200 m/s (a tip Mach number of 0.536) at an advance ratio of 0.55. Fully turbulent Navier-Stokes calculations were performed using AF-CGS for the free stream conditions, an advance ratio of 0.61 and reduced frequency of 0.185, corresponding to the NACA 0012 blade profile at r/R = 0.892.

The development of the flow field over one full rotation of the rotor blade is shown in Figure (10), in which instantaneous contours of pressure are plotted for selected azimuth angles. Initially the flow field is dominated by a rapid expansion of the flow at the aerofoil leading edge, which is a characteristic feature of the flow around the relatively blunt NACA 00XX family of aerofoils. As the incident Mach number is increased a region of high adverse pressure gradient develops towards the aerofoil trailing edge which eventually extends over most of the aerofoil chord. For Mach numbers in the transonic range the favourable effects of an accelerating flow become increasingly evident. In Figures (11a) and (11b) calculated surface pressure distributions are presented which clearly show that for the unsteady flow the shock wave is much weaker than that in the corresponding steady flow. Calculated instantaneous velocity vectors, Figure (12), reveal that at an azimuth angle of 75° the flow separates from the aerofoil surface at the foot of the shock, re-attaching a small distance downstream to form a small separation bubble. As the incident Mach number approaches its maximum value at $\psi = 90°$,the shock wave continues to increase in strength while moving towards the trailing edge of the aerofoil. The corresponding shock induced separation becomes increasingly severe and the separation bubble lengthens, until eventually the re-attachment point moves beyond the aerofoil trailing edge and the flow becomes fully separated.

Although the incident Mach number reaches its maximum value at $\psi = 90°$, the shock wave continues to increase in strength as the flow begins to decelerate. Maximum calculated shock strength occurs at an azimuth angle of 120°, clearly demonstrating the adverse effects of flow deceleration, Figure (11c) is also important in this respect . For azimuth angles beyond 120° the shock wave begins to move towards the aerofoil leading edge diminishing in strength as it does so, until by an azimuth angle of 165° the flow is again wholly subsonic.

The flow on the retreating side of the rotor blade (azimuth angles 180° to 360°) is wholly subsonic and dominated by a characteristic rapid expansion at the leading edge. Figure (10) indicates that for azimuth angles close to 270°, where the incident Mach number is at its minimum value, there is a very weak pressure gradient over most of the aerofoil surface..

The development of the flow field with azimuth angle described above shows good qualitative agreement with the expected physical behaviour of the flow, however a proper validation of the model requires a comparison with experimental measurements. In Figures (13) and (14) the results of the present Euler and Navier-

Stokes calculations are compared with those of Lerat and Sides[6] and the experimental measurements of Phillipe and Chattot[8]. The current Euler calculations show excellent agreement with those of Lerat and Sides, which would seem to indicate that the present inviscid model is correct. Comparison of the present Euler calculation with experiment is fair for azimuth angles in the range 0° to 90° but poor otherwise. Comparison of the present Navier-Stokes calculation with the experimental measurements of Phillipe and Chattot is much improved particularly for azimuth angles in the range 90° to 140°. Such an improvement in the comparison with experiment, for this range of azimuth angles, reveals the importance of shock-boundary layer interactions for this class of flows. The remaining difference between calculation (both Euler and Navier-Stokes) and experimental measurements are thought to be due the three dimensional effects which are present in the experiment. In the absence of suitable two dimensional test data it is unlikely that any further improvements in validation can be made.

7. Conclusions.

A method for the solution of the thin layer Navier-Stokes equations for the flow field around aerofoils undergoing inplane oscillations has been presented. The present Euler calculations are encouraging and follow the flow physics as we would expect. The current Euler calculations show fair agreement with three dimensional experimental measurements for azimuth angles 0° to 90° and with the Euler calculations of Lerat and Sides, while for azimuth angles 90° to 120° agreement between calculation and experiment is poor.

Fully turbulent Navier Stokes calculations show significant improvements when compared with the experimental data which is thought to indicate the importance of shock-boundary layer interactions for this class of flows. It is believed that the differences which remain are due, in the main, to three dimensional effects which are not currently modelled. In the absence of high speed experimental test data for this class of flows it is unlikely that the method can be validated further.

Experience with AF-CGS has shown that the method is insensitive to most of the main parameters. It has been found that the choice of time step is determined from a consideration of the efficiency of the linear solver and not by accuracy as would be expected. The current method is sensitive to grid refinement, it is thought that this is due to the unsteady motion of the shock wave and it is suggested that local grid redistribution should be used to refine the grid in regions of high density gradient.

Work is now required to extend the current numerical approach to three dimensions.

References

1. Maresca C.
   Favier C.
   Rebont J.
   Experiments on aerofoil at high angles of incidence in longitudinal oscillations.
   Journal of Fluid Mechanics V.92 pt 4 June 1979.

2. Favier C.
   Bellendy J.
   Maresca C.
   Influence of coupling incidence and velocity fluctuations on the aerofoil dynamic stall.
   American Helicopter Society 48th Annual Forum, Washington D.C. June 1992.

3. Favier, D.
   Agnes, A.
   Barbi, C.
   Maresca, C.
   Combined translation/pitch motion: A new aerofoil - dynamic stall simulation
   Journal of Aircraft V.25 September 1988.

4. Van der Waal, B.
   Leischmann, J.
   Influence of variable flow velocity on unsteady aerofoil.
   18th European Rotorcraft Forum, September 1992.

5. Habibie, I.
   Laschka, B.
   Weishaupl, C.
   Analysis of unsteady flows around wing profiles at longitudinal accelerations.
   ICAS 1994.

6. Lin, C.
   Pahlke, K.
   Numerical solution of the Euler equations for aerofoils in arbitrary unsteady motion.
   Aeronuatical Journal V.98 June/July 1994.

7. Lerat, A.
   Sides, J.
   Numerical simulation of unsteady transonic flows using the Euler equations in integral form.
   Onera Technical Report TP 1979-10 1979.

8. Phillipe, J.
   Chattot, J.
   Experimental and theoretical studies on helicopter rotor blades at Onera.
   Onera Technical Report TP 1980-96 September 1980.

9. Badcock, K.
   The AFCGS aerofoil code: Theory and user guide.
   Glasgow University Technical Report.

10. Badcock, K.
    An efficient unfactored implicit method for aerofoil flows.
    Glasgow University Technical Report, Aero 93 March 1993.

11. Baldwin, B.
    Lomax, H.
    Thin layer approximation and algebraic model for separated turbulent flows.
    AIAA Report 78-0257 January 1978.

12. Osher, S.
    Solomon, F.

Upwind difference schemes for hyperbolic systems of conservation laws.
Mathematics of computation V.38 No.158 1982.

13. Van Leer, B.

A second order sequel to Gudonovs method.
Journal of computational physics V.32 pp 101-36.

14. Orkwis, P.
    Vanden, K.

On the accuracy of numerical vs analytical Jacobians.
AIAA Report 94-0176 January 1994.

15. Sonneveld, P.

CGS: A fast Lanczos type solver for non-symmetric linear systems.
SIAM Journal statistics and computation V.10 pp 36-52 1989.

16. Beam, R.
    Warming, R.

An implicit factored scheme for the complete Navier-Stokes equations.
AIAA Journal V.16 pp 393-402 1978.

17. Gaitonde, A.
    Fiddes, S.

A three dimensional moving mesh method for the calculation of unsteady transonic flows.
Aeronautical Journal V.99 April 1995.

18. Qin, N.
    Richards, B.E.

Finite volume 3D Navier-Stokes and parabolised Navier-Stokes solution of hypersonic viscous flow around a delta wing using Osher's flux difference splitting.
Proceedings of Workshop on Hypersonic flow for re-entry problem, Vol.2 pp 947-59. Springer-Verlag 1992.

19. Qin, N.

A comparative study of two upwind methods as applied to Navier-Stokes equations fo resolving boundary layers in visccous flows.
Glasgow University Technical report AERO-9120, 1991.

20. Qin, N.
    Soriba, K.W.
    Richards, B.E.

Shock-Shock, Shock-Vortex interactions and aerodynamic heating in hypersonic corner flow.
Aeronautical Journal V.95 pp 152-160 1991.

Figure (1) Effect of time step on solution accuracy.

Lift coefficient (based on average velocity).

Azimuth angle (degrees)

100 iterations/cycle
400 iterations/cycle
600 iterations/cycle
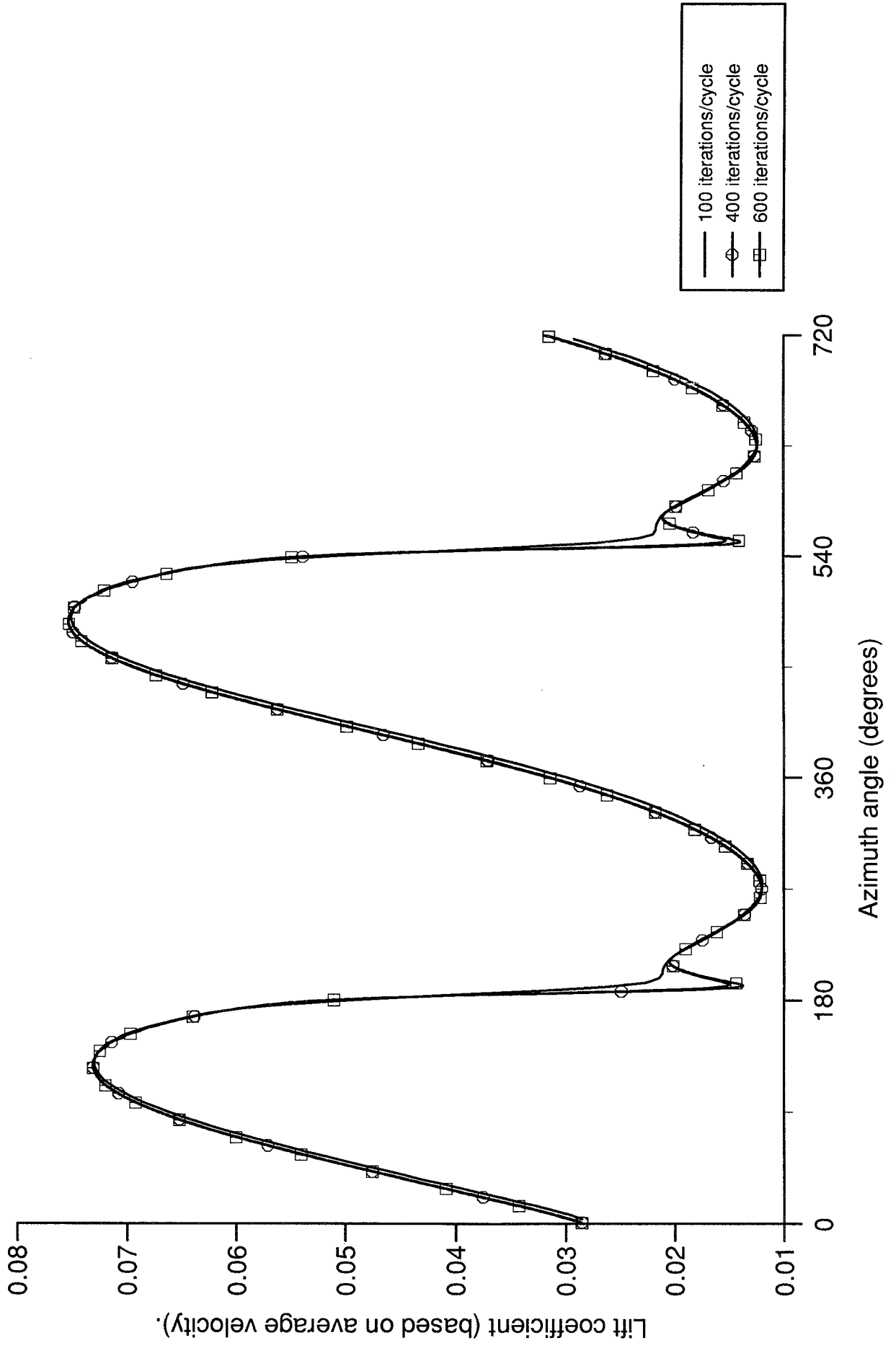
Figure (2) Number of CGS iterations required to meet a given solver tolerance.
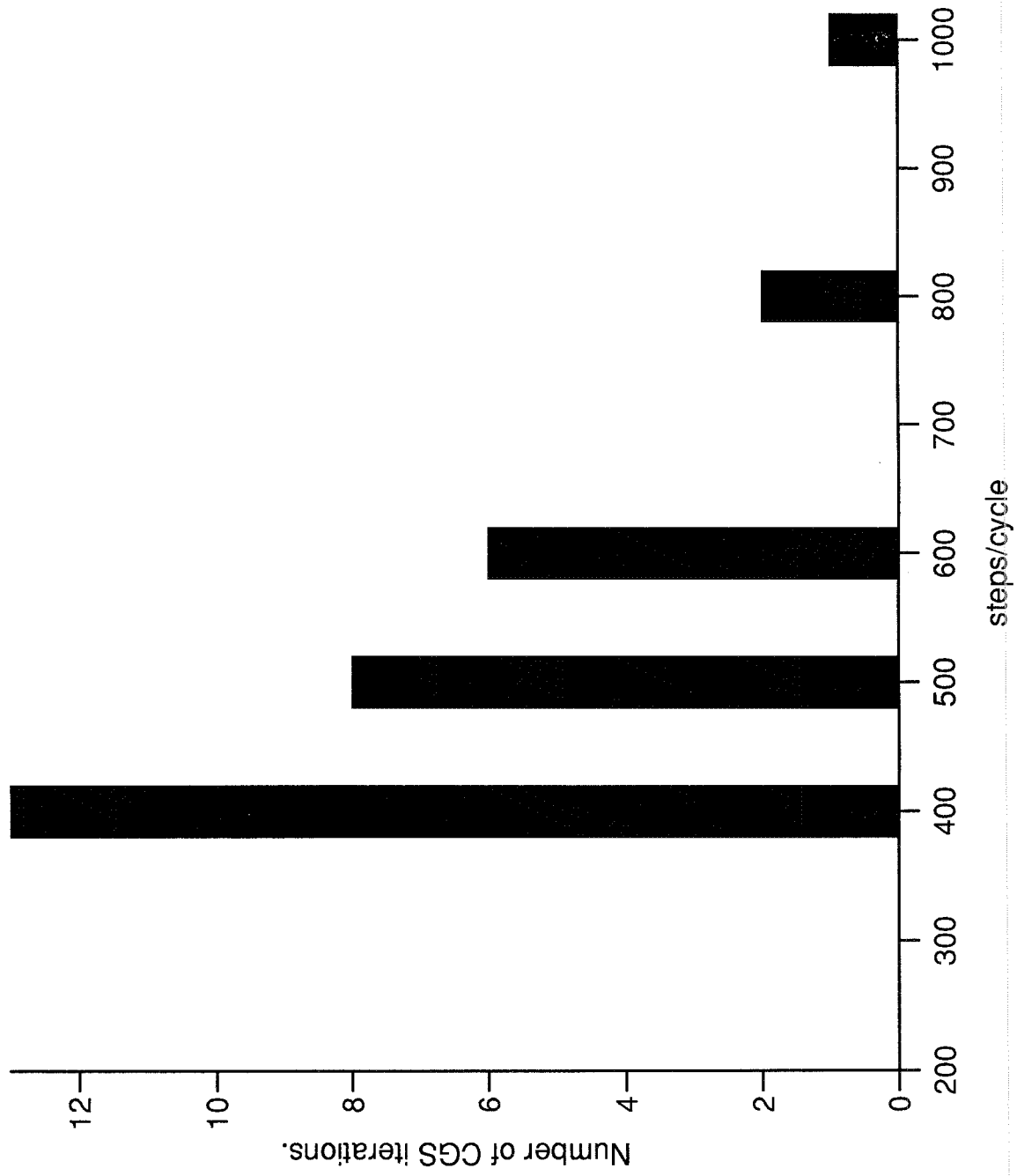
Figure (3) CPU time required for two full cycles of the aerofoil motion.
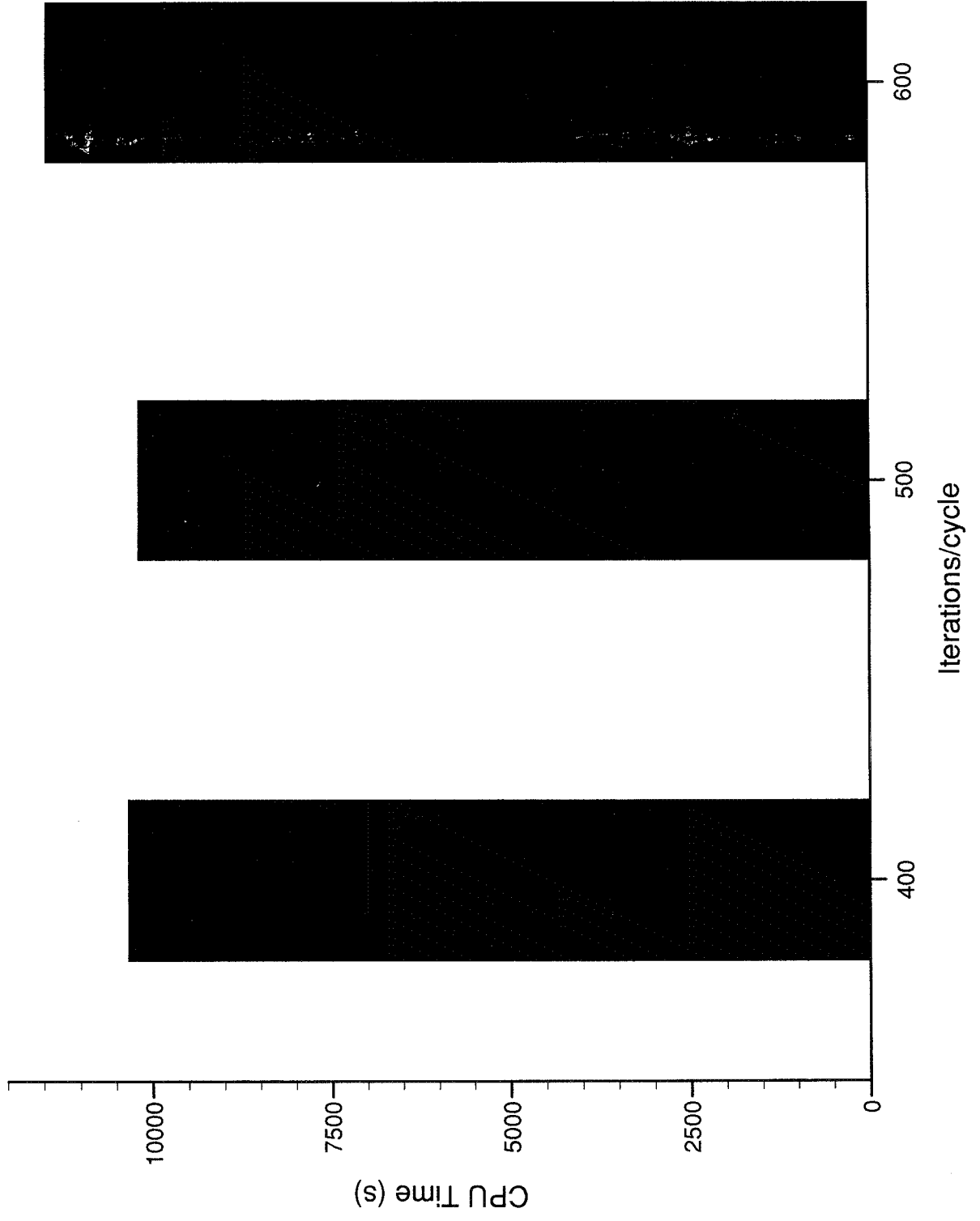
Figure (4) Influence of convergence tolerance on calculated results.

Cl (based on avergae velocity).

Azimuth angle (degrees).

Tolerance (||r||/||b||)
0.100
0.010
0.001
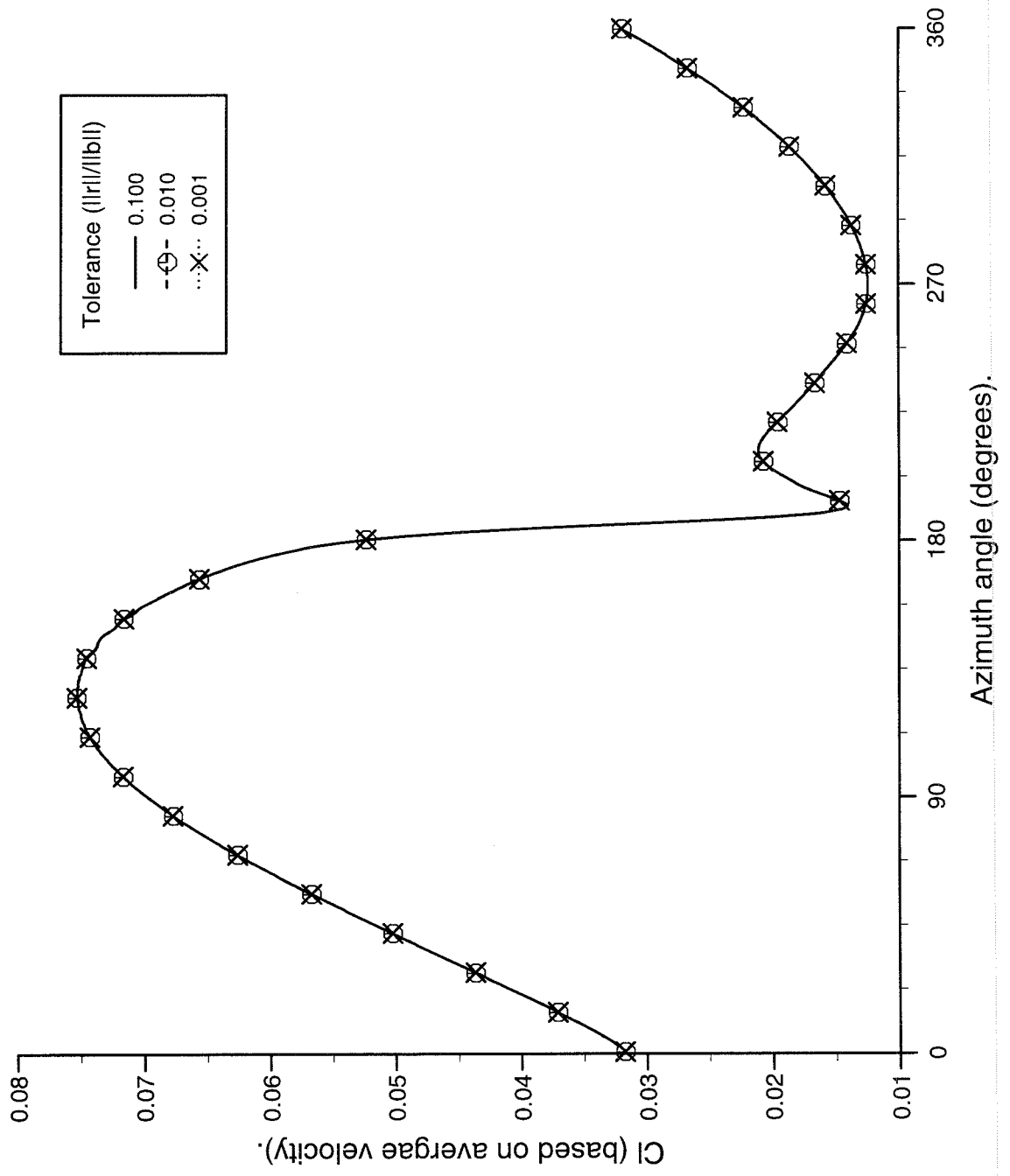
Figure(5) Influence of solver tolerance on calculated results.

Cl (based on average velocity).

Azimuth angle (degrees).

Tolerance (||r||/||b||)
——— 0.00500
—□— 0.00050
········ 0.00005
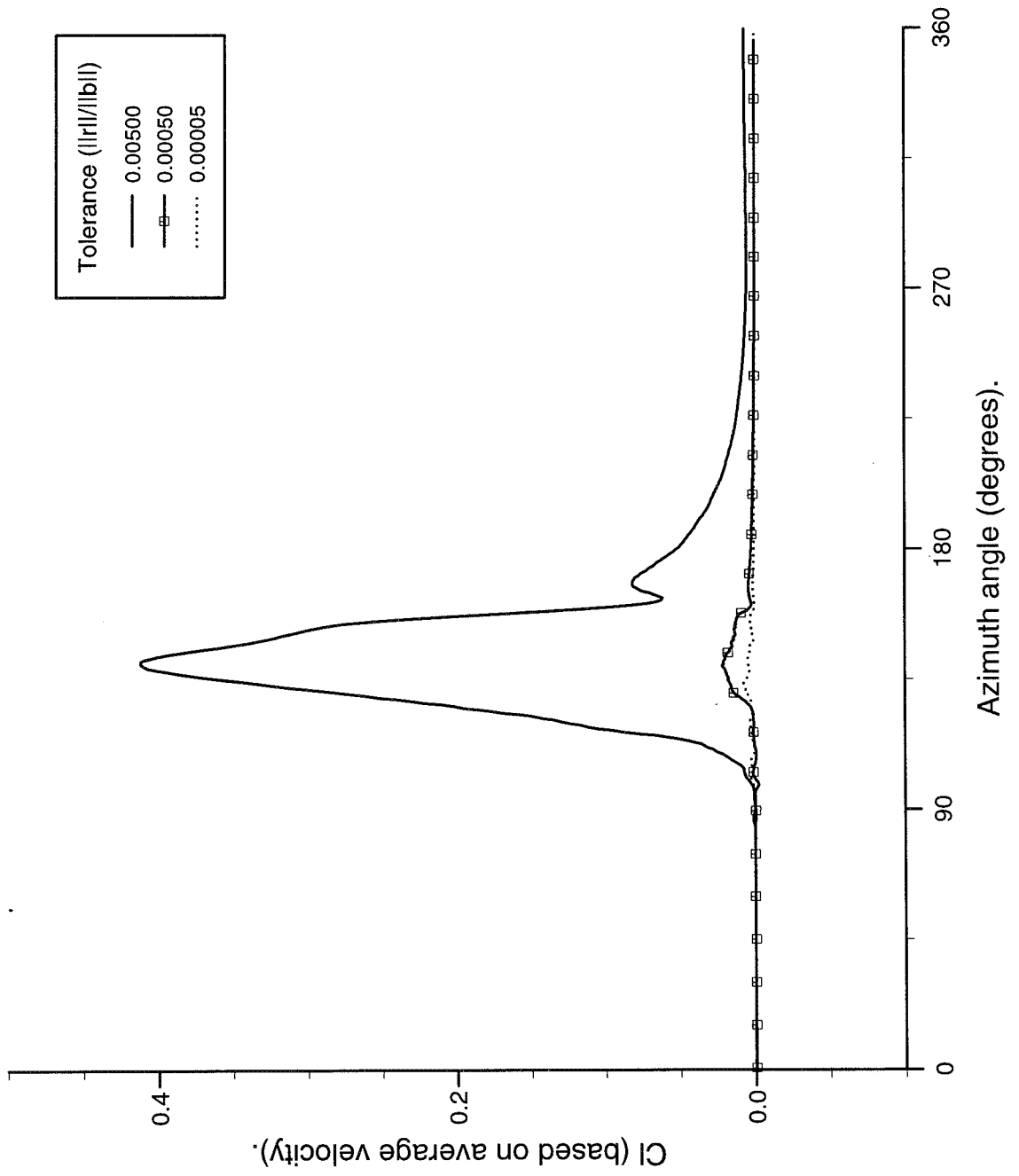
Figure (6) Influence of grid density on calculated lift coefficient.
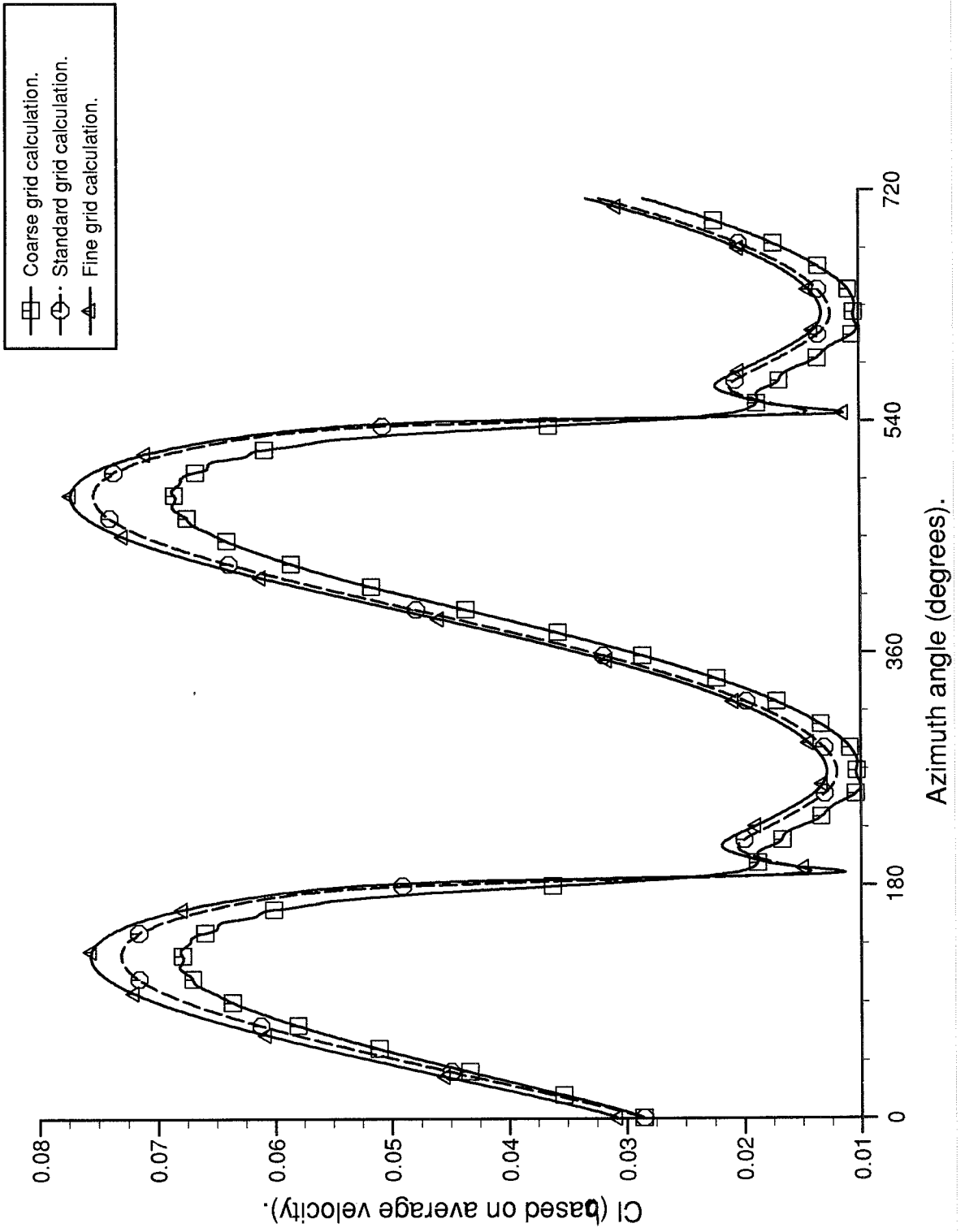
Figure (7) Influence of farfield boundary location on calculated results.

Cl (based on average velocity).

Azimuth angle (degrees).

Farstream boundary position:

——— 20 chord lengths.
- - - - 40 chord lengths
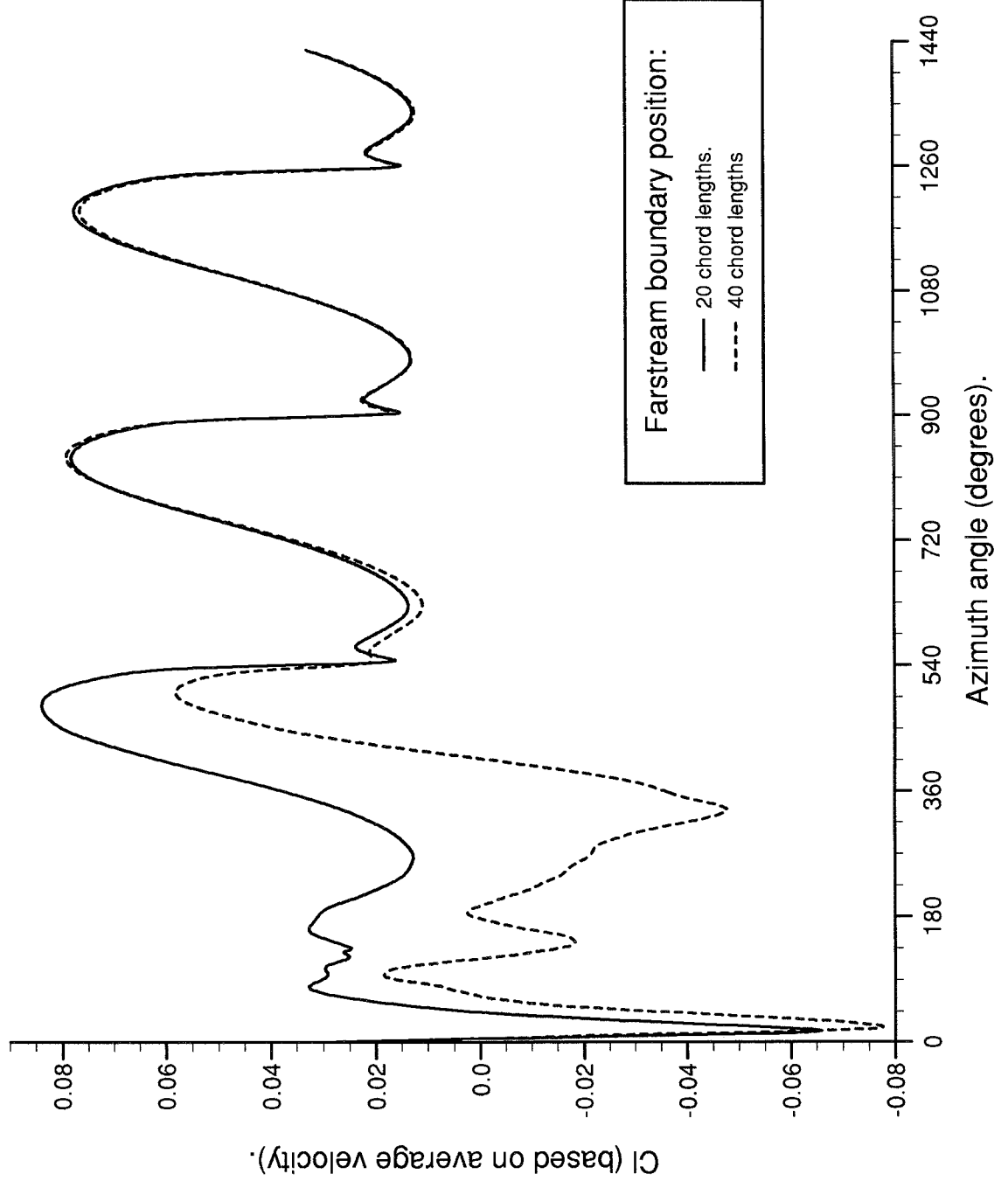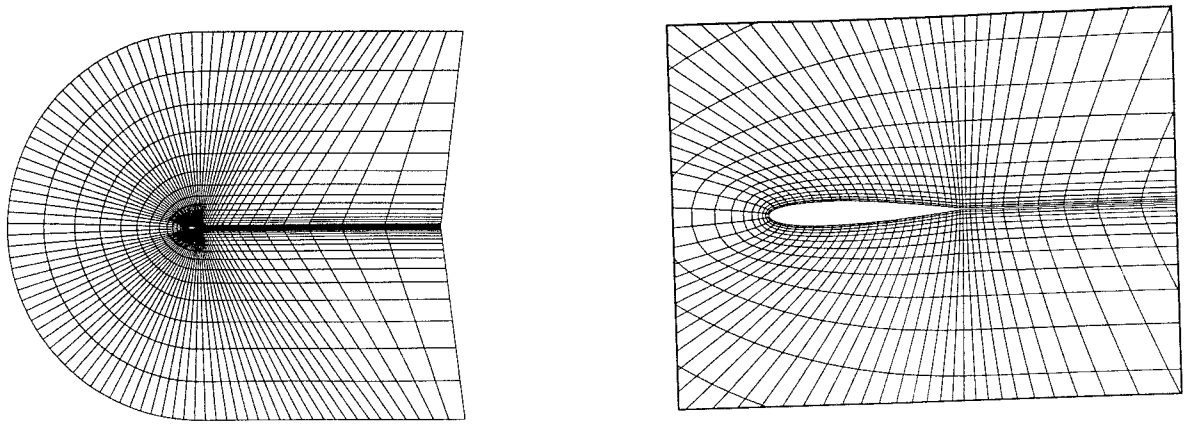
(a) Coarse grid (101 x 24).
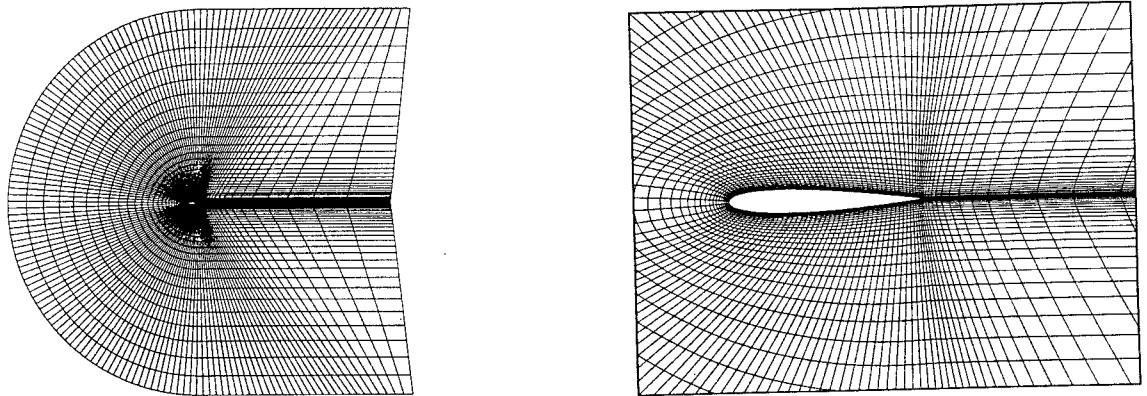
(b) Standard grid (153 x 48).
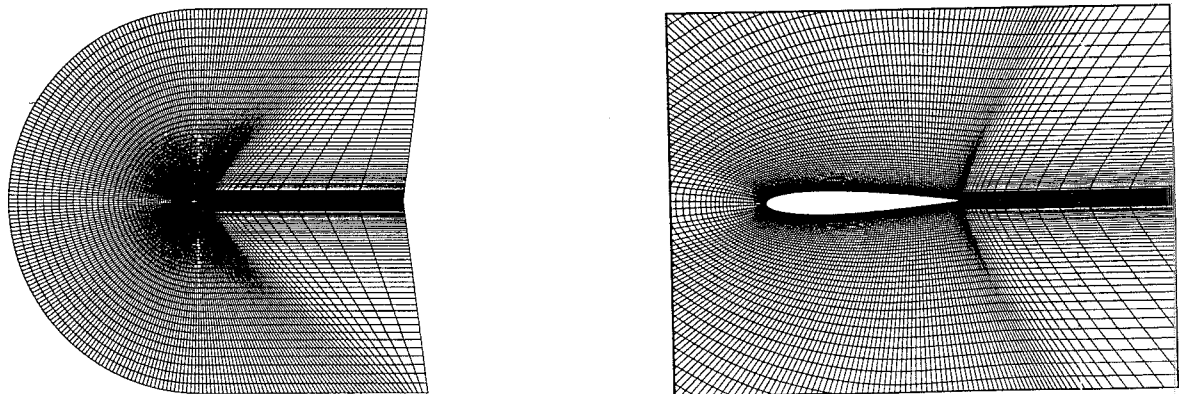
(c) Fine grid (259 x 96).

Figure (8) Computational grids used for Euler calculations.
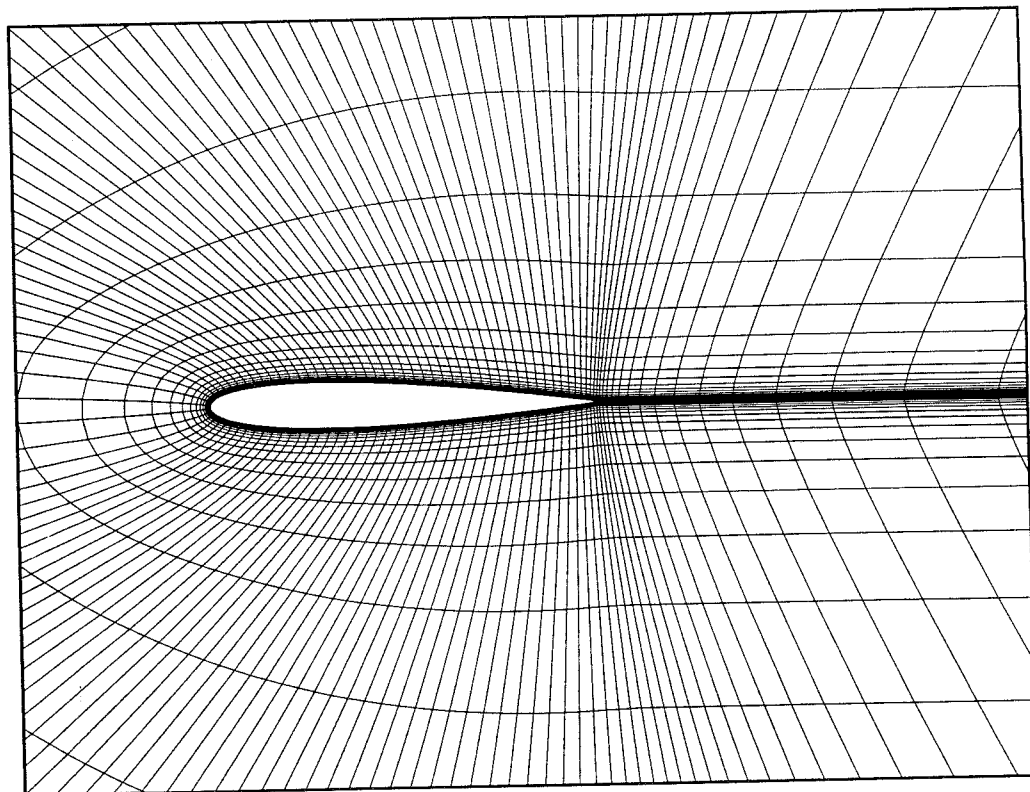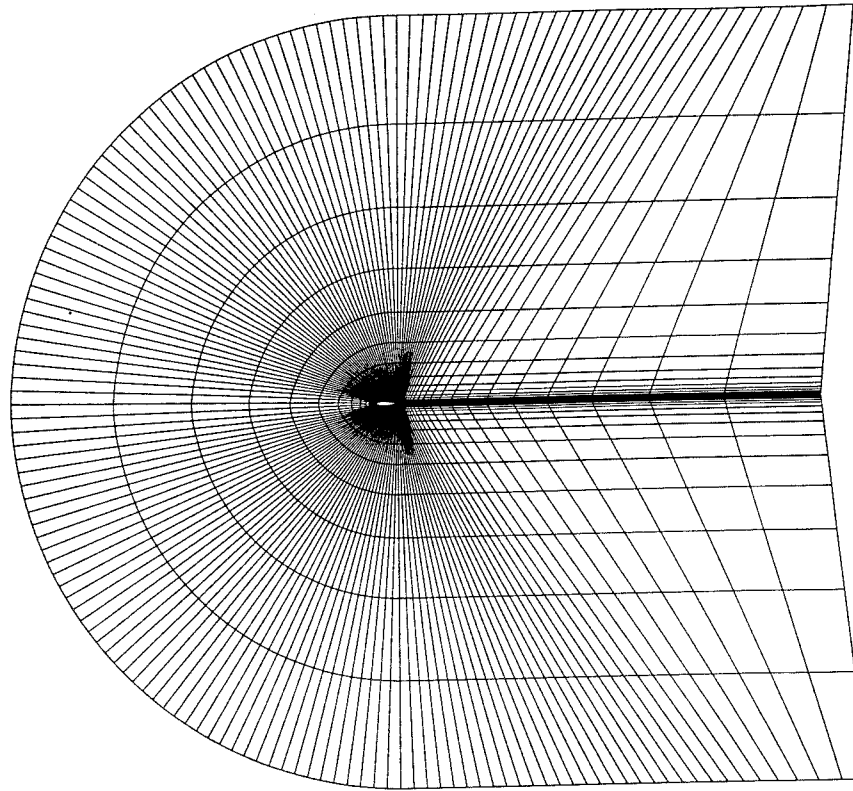
Figure (9) Computational grid used for Navier-Stokes calculations.

(a) ψ = 0°   (b) ψ = 15°

(c) ψ = 30°   (d) ψ = 45°

(e) ψ = 60°   (f) ψ = 75°
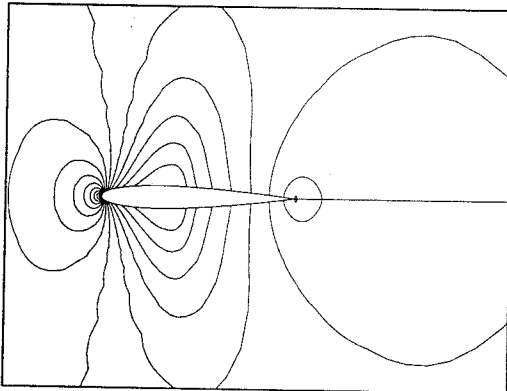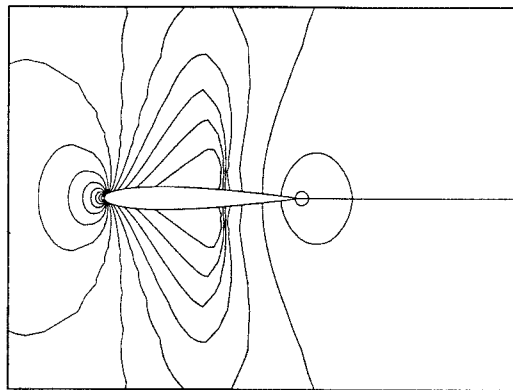
(g) ψ = 90°   (h) ψ = 105°

Figure (10) Instantaneous local pressure contours.

(i) ψ = 120°   (j) ψ = 135°

(k) ψ = 150°   (l) ψ = 165°

(m) ψ = 180°   (n) ψ = 210°
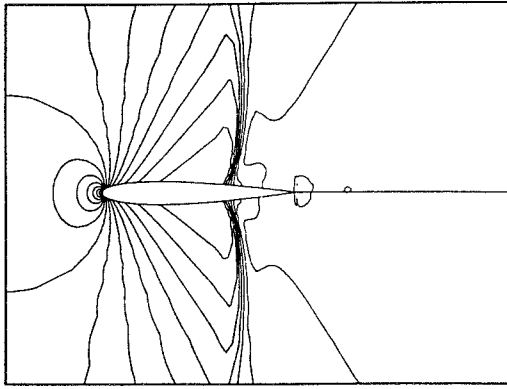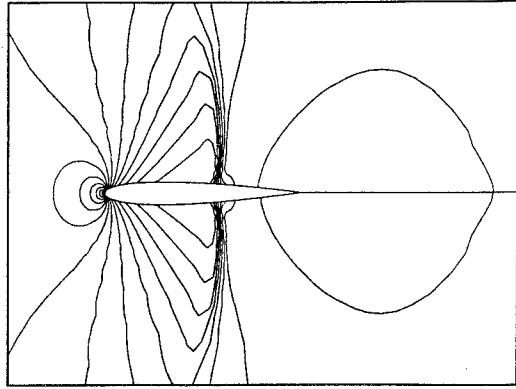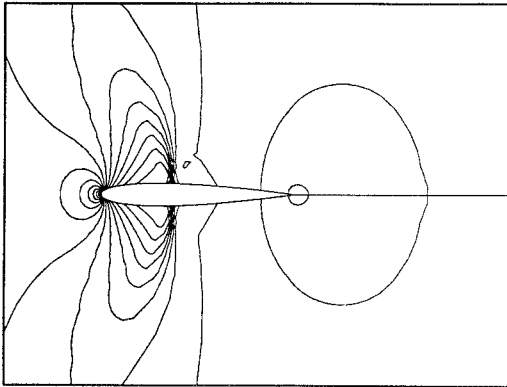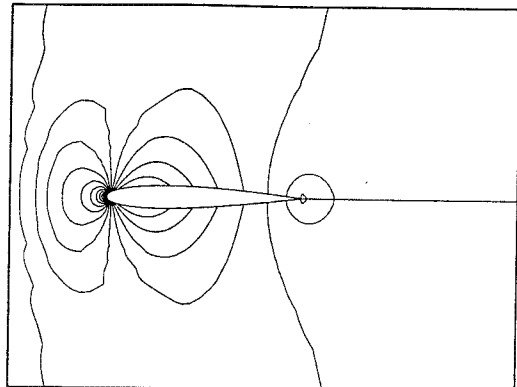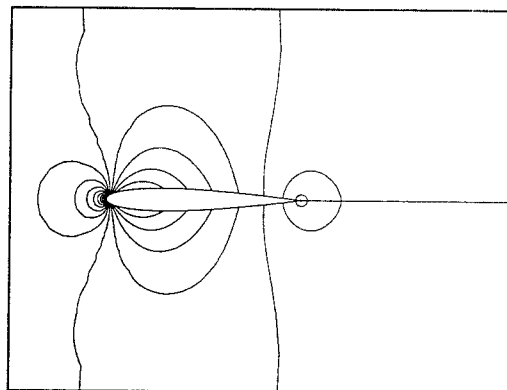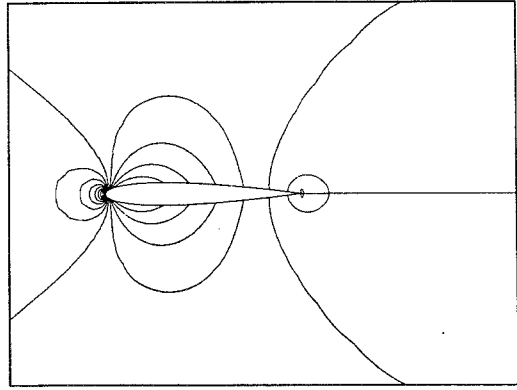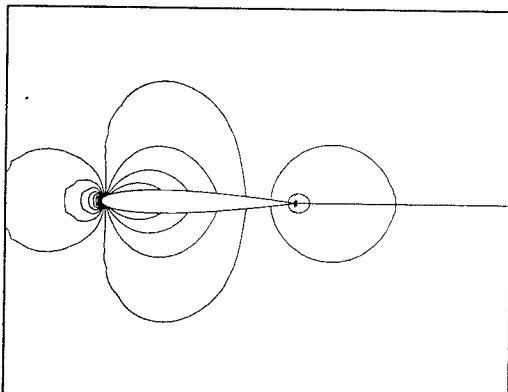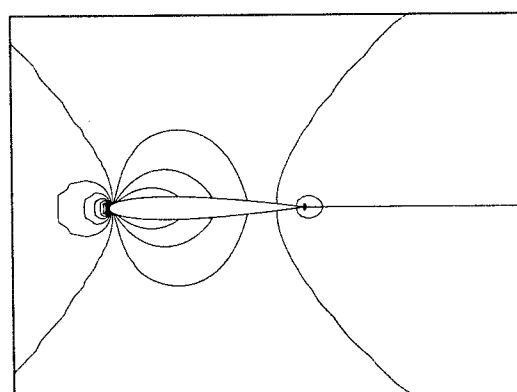
(o) ψ = 240°   (p) ψ = 270°

Figure (10) continued.

(q) ψ = 300°

(a) ψ = 60°

(r) ψ = 330°

(b) ψ = 90°

(c) ψ = 120°
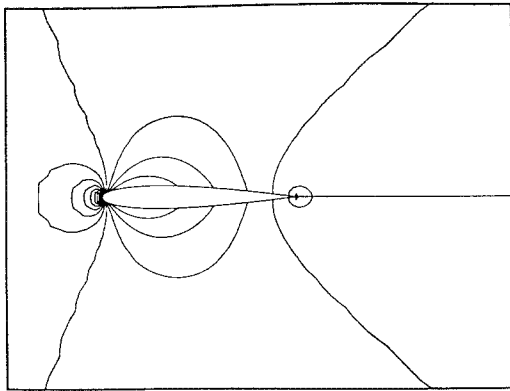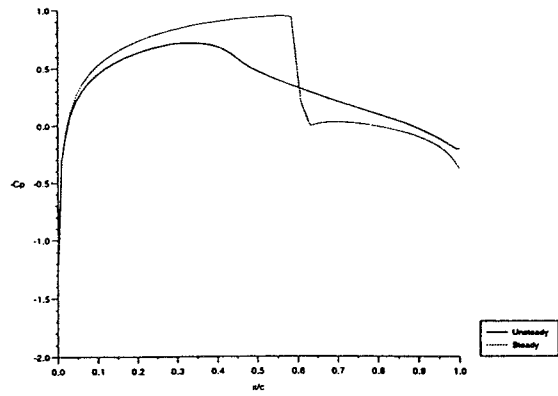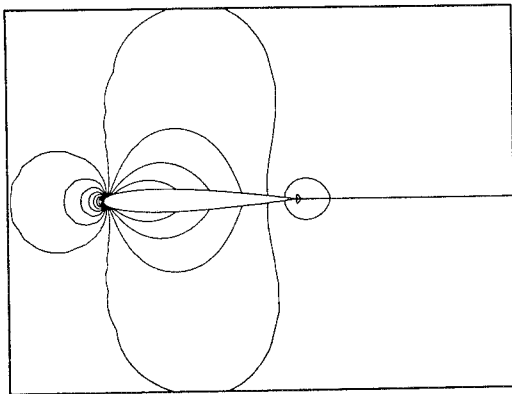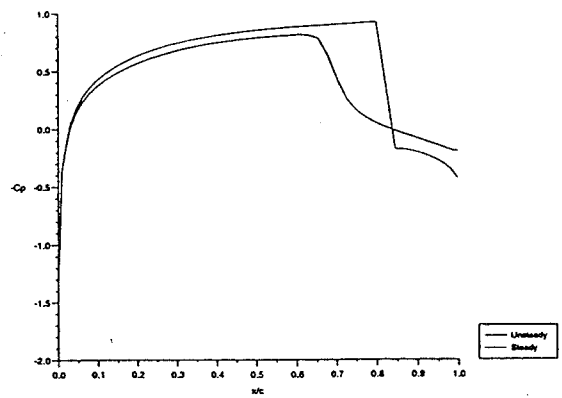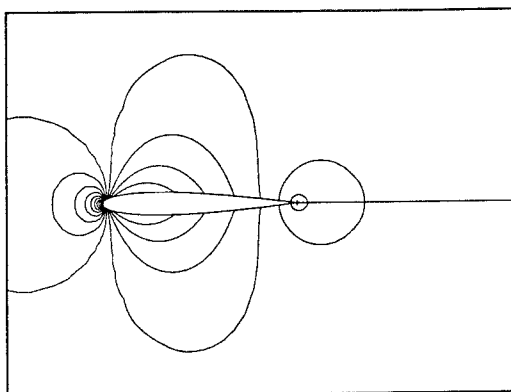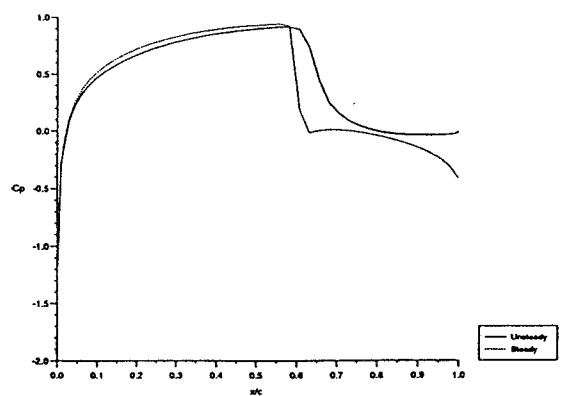
(s) ψ = 360°

Figure (10) Concluded.

Figure (11) Instantaneous surface
Pressure distributions.
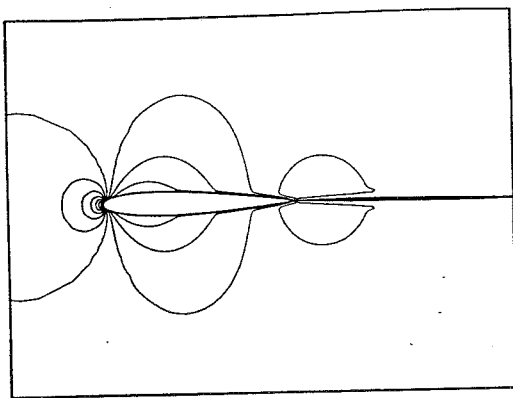
(a) $\psi = 0°$
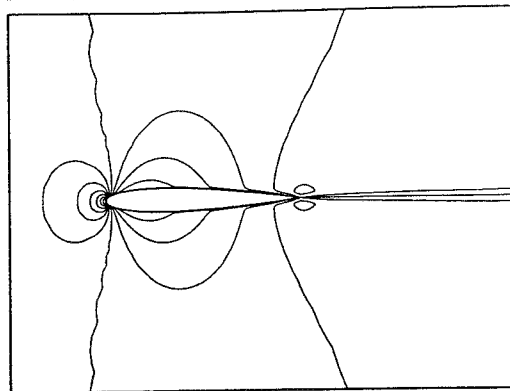
(b) $\psi = 15°$
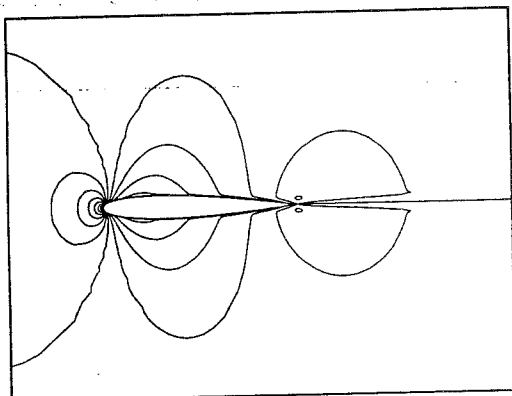
(c) $\psi = 30°$
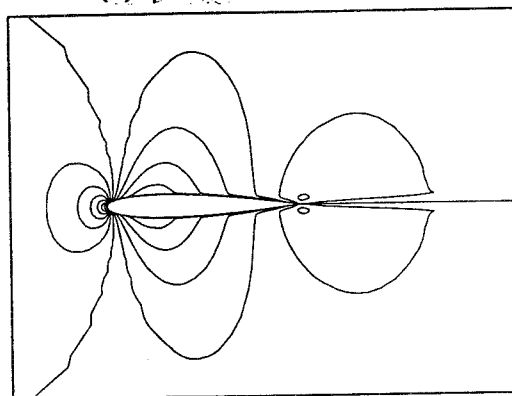
(d) $\psi = 45°$
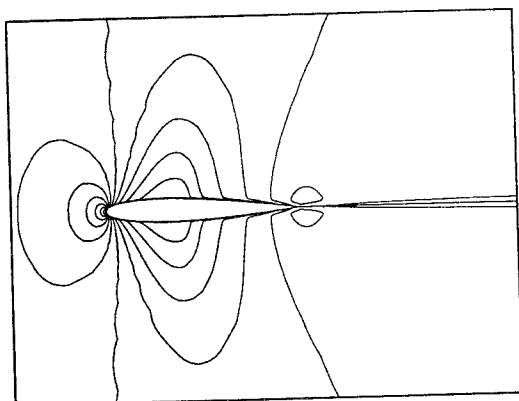
(e) $\psi = 60°$
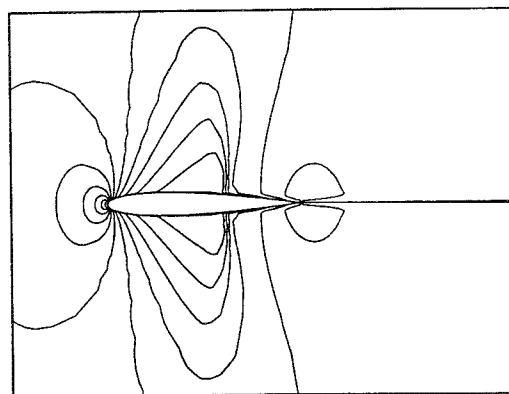
(f) $\psi = 75°$
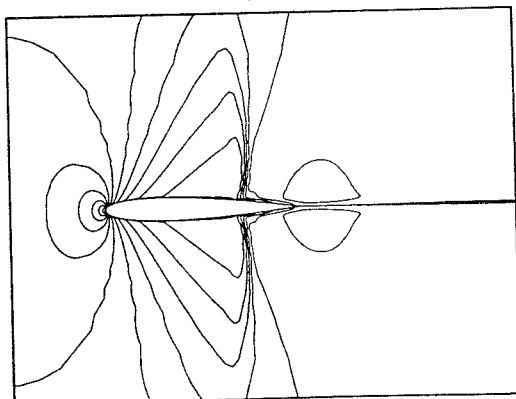
(g) $\psi = 90°$
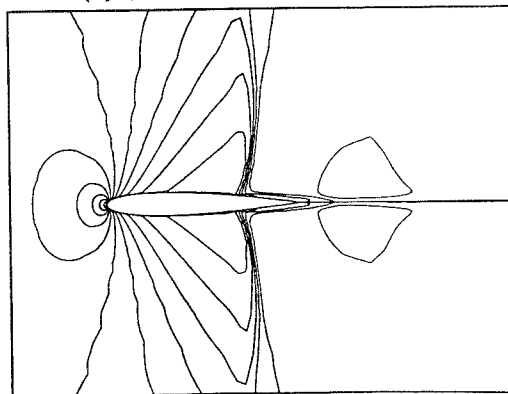
(h) $\psi = 105°$

Figure (12) Instantaneous density contours.

(i) ψ = 120°

(j) ψ = 135°

(k) ψ = 150°

(l) ψ = 165°

(m) ψ = 180°

(n) ψ = 210°

(o) ψ = 240°
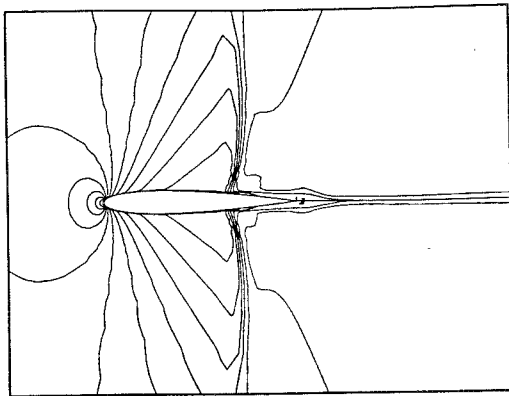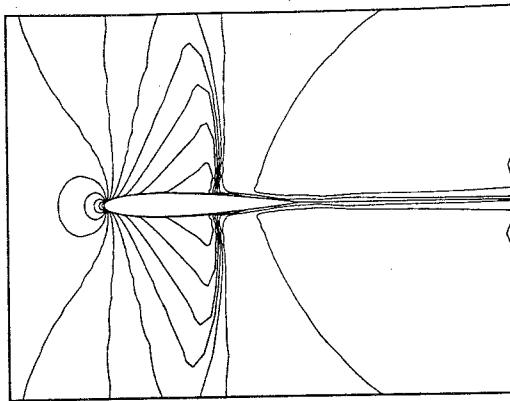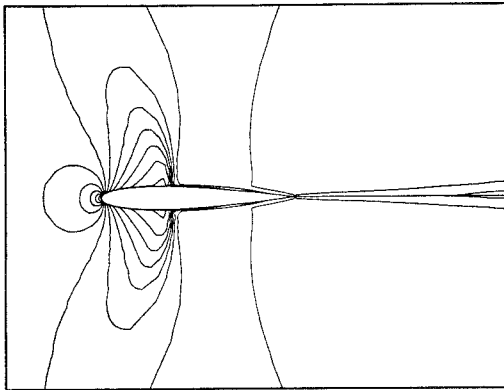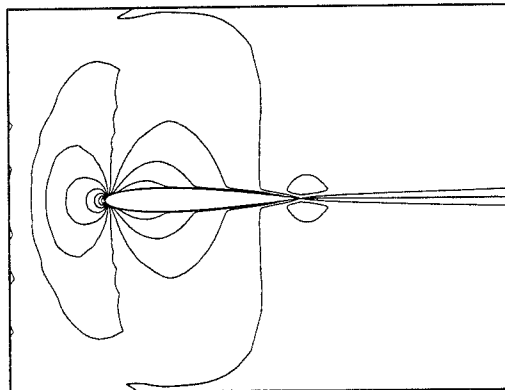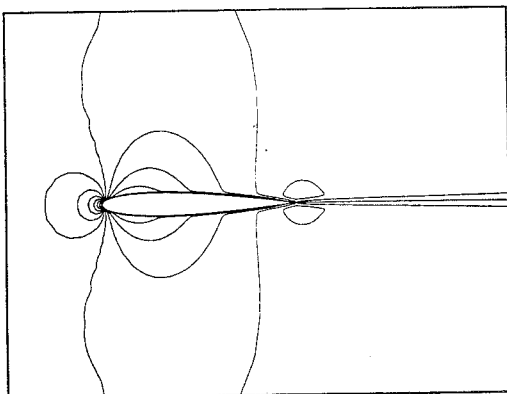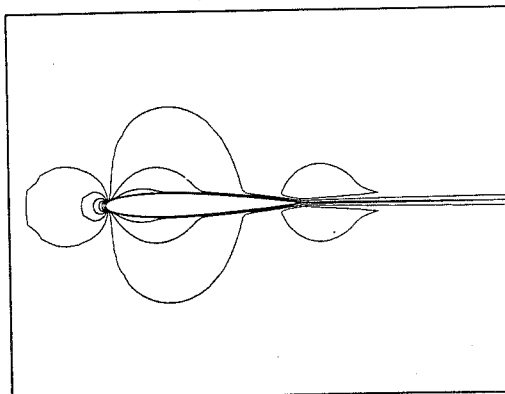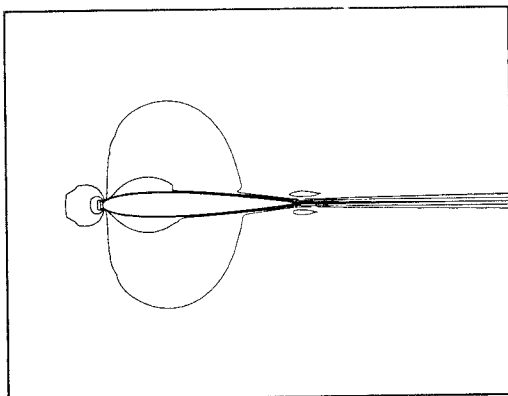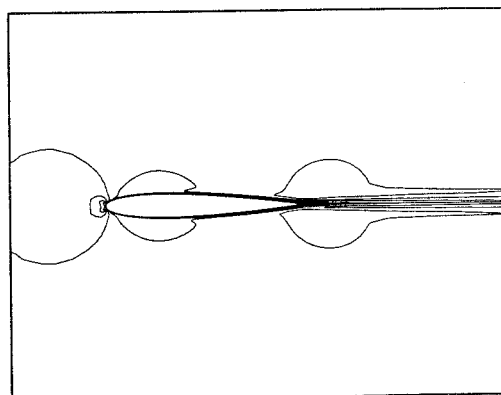
(p) ψ = 270°

Figure (12) Continued.

(q) ψ = 300°

(r) ψ = 330°
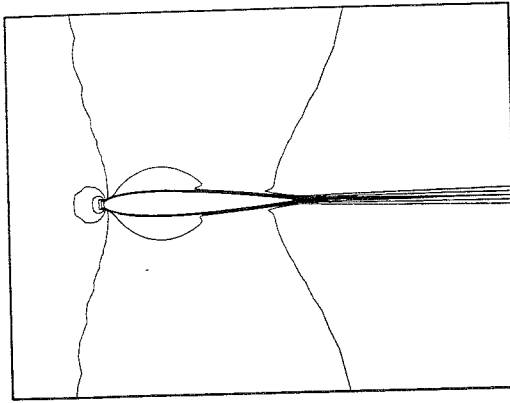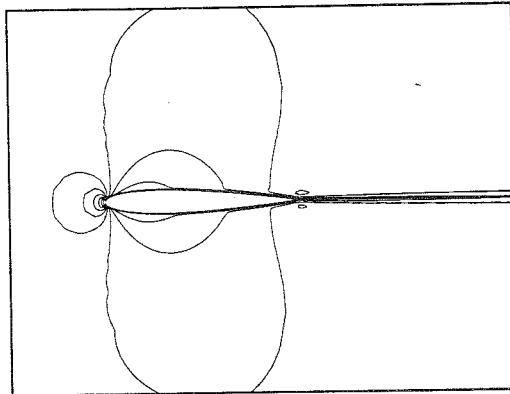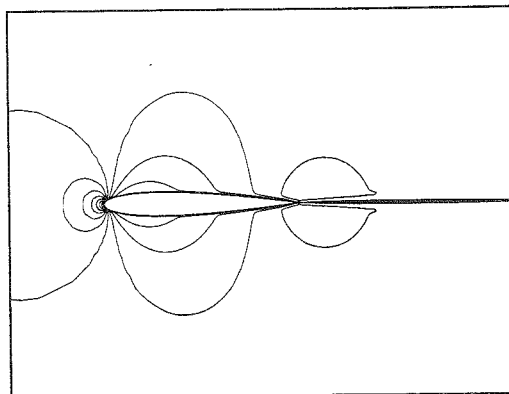
(s) ψ = 360°

Figure (12) Concluded.

Figure (13) Comparison of Euler calculation with Lerat and Sides (Ref. 9).

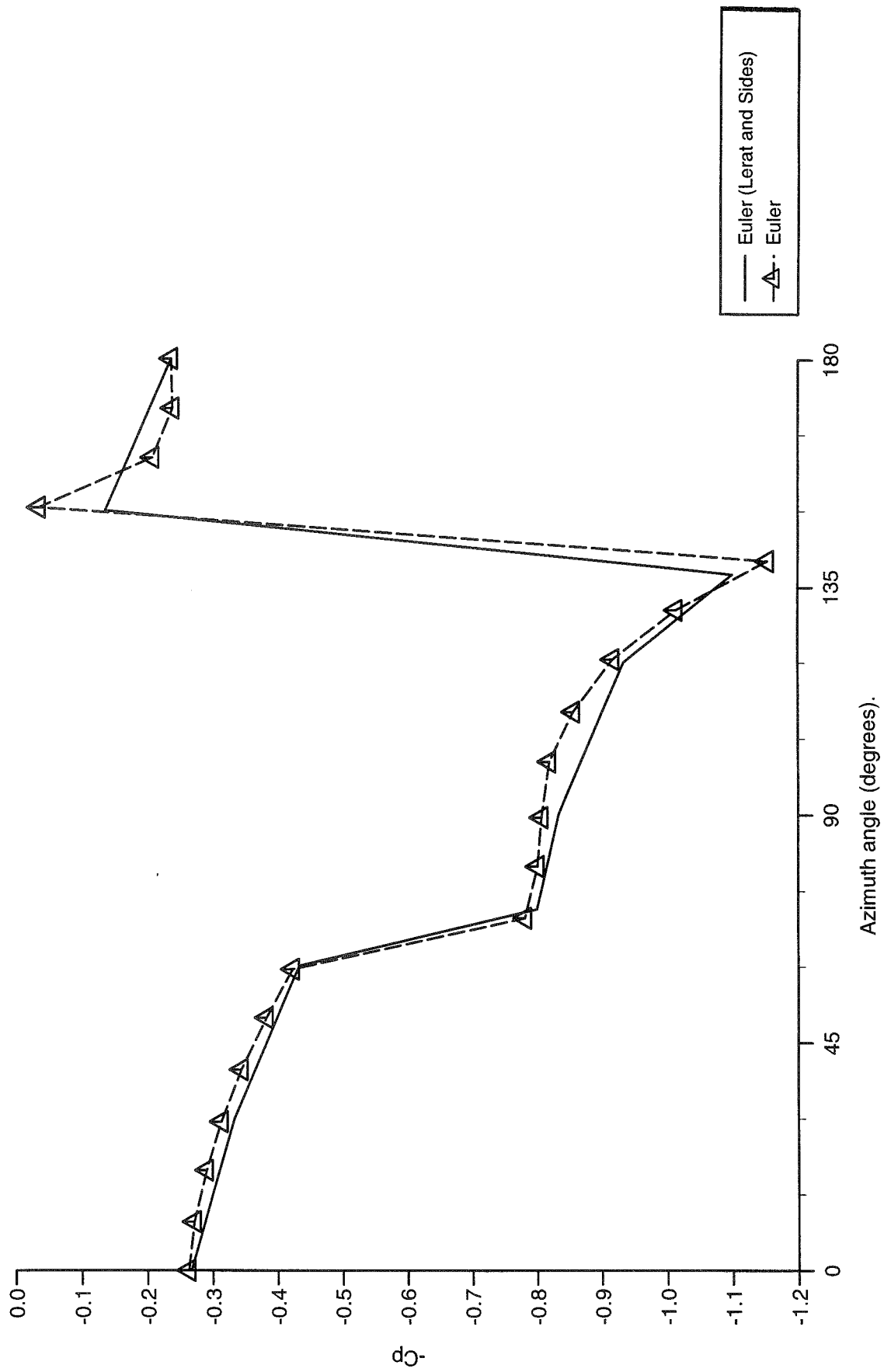Azimuth angle (degrees).

Legend:
— Euler (Lerat and Sides)
—△— Euler

Figure (14) Comparison of present calculations with experiment.